Experimental validation of damping properties and solar pressure effects on flexible, High Area-to-Mass Ratio debris model

Sittiporn Channumsin Matteo Ceriotti, Gianmarco Radice and Ian Watson

Geo-Informatics and Space Technology Development Agency (GISTDA), Bangkok 10210, Thailand

School of Engineering, University of Glasgow, Glasgow G12 8QQ, United Kingdom

sittiporn@gistda.or.th matteo.ceriotti@glasgow.ac.uk Gianmarco.Radice@glasgow.ac.uk Ian.Watson@glasgow.ac.uk

ABSTRACT

Multilayer insulation (MLI) is a recently-discovered type of debris originating from delamination of aging spacecraft; it is mostly detected near the geosynchronous orbit (GEO). Observation data indicates that these objects are characterised by high reflectivity, high area-to-mass ratio (HAMR), fast rotation, high sensitivity to perturbations (especially solar radiation pressure) and change of area-to-mass ratio (AMR) over time. As a result, traditional models (e.g. cannonball) are unsuitable to represent and predict this debris' orbital evolution. Previous work by the authors effectively modelled the flexible debris by means of multibody dynamics to improve the prediction accuracy. The orbit evolution with the flexible model resulted significantly different from using the rigid model. This paper aims to present a methodology to determine the dynamic properties of thin membranes with the purpose to validate the deformation characteristics of the flexible model. A high-vacuum chamber (10^{-4} mbar) to significantly decrease air friction, inside which a thin membrane is hinged at one end but free at the other provides the experimental setup. A free motion test is used to determine the damping characteristics and natural frequency of the thin membrane via logarithmic decrement and frequency response. The membrane can swing freely in the chamber and the motion is tracked by a static, optical camera, and a Kalman filter technique is implemented in the tracking algorithm to reduce noise and increase the tracking accuracy of the oscillating motion. Then, the effect of solar radiation pressure on the thin membrane is investigated: a high power spotlight (500-2000 W) is used to illuminate the sample and any displacement of the membrane is measured by means of a high-resolution laser sensor. Analytic methods from the natural frequency response and Finite Element Analysis (FEA) including multibody simulations of both experimental setups are used for the validation of the flexible model by comparing the experimental results of amplitude decay, natural frequencies and deformation. The experimental results show good agreement with both analytical results and finite element methods.

Keywords: High area-to-mass ratio debris; Deformation model; Flexible model; Multilayer insulation; Multibody model; Damping ratio and Validation.

1. INTRODUCTION

A new population of space debris type in Geostationary synchronous orbit (GEO), with high area-to-mass ratio (HAMR) and extremely sensitive to perturbations (especially non-conservative perturbations) was detected in 2004 by Schildknecht et al. [1-3]. Multilayer insulation (MLI) that has delaminated from spacecraft is assumed to be a possible source of these debris objects [4-6]. The basic substrate of MLI (PET®, Kapton® and Teflon®) is coated with very thin metal (aluminium, gold or silver on one or both sides of substrate) with thickness of the order of 1000 Á. The important features of MLI are very low weight, high flexibility, and low outgassing properties under vacuum environment.

HAMR objects, approximated to a cannonball model, where the area-to-mass ratio (AMR) is assumed to be constant and attitude motion neglected, have been studied in GEO under perturbations over long term periods. Results show that the inclination varies proportionally to the magnitude of the AMR values [7-10].

The cannonball model may however not be suitable for HAMR objects: real measurements indicate that the AMR, which is directly proportional to solar radiation force, is not stable but changes over time and the object is likely to display fast attitude motion [11]. Further investigation by Früh et al. [12-14] coupled the orbital and attitude dynamics modelling of the debris as a rigid flat plate and a curled plate. Solar radiation pressure is shown to affect, the orbital evolution of these objects even over short periods and attitude motion, even when averaged, needs to be considered together with orbital motion for an accurate propagation of the motion of the HAMR object.

Nevertheless, all studies mentioned above assume the HAMR objects to be rigid bodies. Their constant AMR however leads to less accurate propagation of the orbital evolution for this debris type. A more accurate modelling of the actual shape over the orbital period, therefore, will provide more precise orbital evolution. McMahon et al [15] studied the solar radiation effects on variable shapes: the HAMR model is here represented through one of five discrete configurations. The type of configuration depends on the spin rates of the object. This investigation highlights that the cannonball is not suitable to approximate the orbital dynamics of this type of debris and supports the fact that the SRP torque highly affects the fast attitude dynamics. A limitation of this study is that this model represents a set of discrete configuration rather than a continuously-deforming object during the time of propagation.

An accurate modelling of the shape of the HAMR debris will provide a more precise orbital prediction as relatively small changes in the effective AMR strongly effect on the orbital evolution of HAMR objects. Finite Element Analysis (FEA) can provide highly accurate shape dynamics but when integrated by numerical propagation, the computational cost becomes prohibitive due to infinite Degree of Freedom (DoF). Previous work by the authors [16], models the flexible membranes, as a series lump masses, connected through rigid rods. Each lump mass consists of rotational springs and dampers to model the flexibility of the thin membrane and represents the folding lines, which are all parallel to each other and the plane is one perpendicular to the membrane itself (2D deformation). The fundamental idea is that SRP depends on the reflection properties of exposed surface and the attitude of an object. Therefore, the shape of the flexible model is not required to be described completely and it is sufficient to find the incident Sun angle. The actual SRP force on the body can be then computed by integrating the pressure on each surface element exposed to solar radiation. This approximates the deformation of the thin, lightweight and HAMR object, using a reasonable amount of computational power to predict orbital dynamics. The results show the irregular and fast rotation dynamics including the continuously changing shape at each time step of the propagation. Solar radiation pressure significantly disturbs the orbital dynamics, generating unstable attitude motion that leads to deformation of the model.

In order to determine the bending stiffness and damping of the actual membrane and validate the flexible model [16], this paper presents an experimental set up and the results from two experiments. The first is a free motion experiment, that uses a swinging membrane in a pendulum-like configuration in a vacuum environment to determine the natural frequency and damping characteristics of the real membrane [17, 18]. A second experiment (radiation pressure experiment) is performed with a high power spotlight, representing solar radiation pressure, on a sample and measuring the ensuing displacement. Results from both experiments will be compared to both simulation of the multibody model and finite element analysis (FEA) through commercial FEA software (ANSYS®).

2. MULTIBODY MODEL

The multibody, flexible model is represented as three lump masses connected with rigid rods ($L = L_1 = L_2 = 0.10$ m). The 2nd lump mass includes a rotational spring and damper. The multibody model used in both free motion and radiation pressure experiments in Fig. 1 is fixed at one end to the top of the vacuum chamber while the another end is left to swing freely under the effects of gravity and other external forces. This 3D membrane is modelled as two dimensional, considering only the plane of the main oscillation. This plane is perpendicular to the plane of the undeformed membrane itself. This means that we assume any torsional deformation and bending outside of this plane as null. The first lump mass is defined as the origin of the frame of reference at the pivot point.

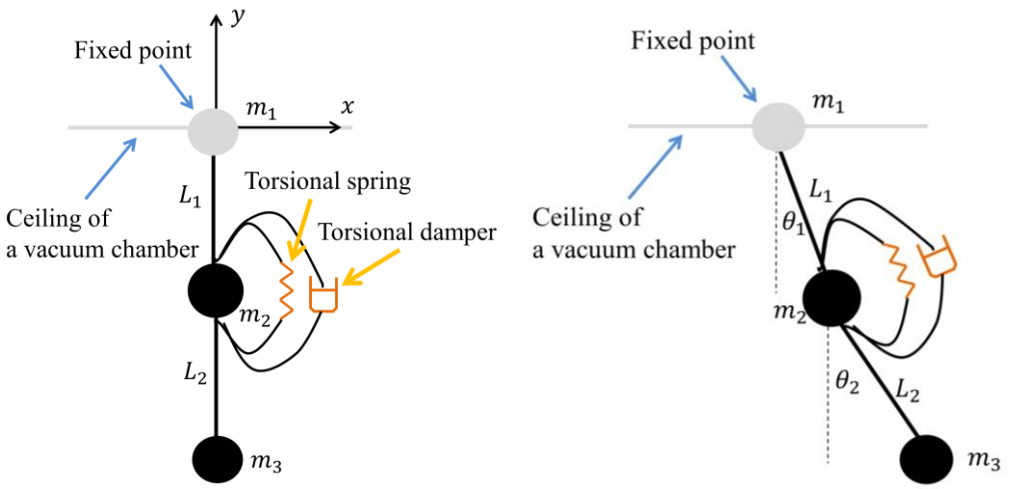

Fig. 1 Multibody model of the three lump masses a) initial position b) Displacement after applying an external force on each lump mass.

In order to develop the dynamics of the system, we first define the positions of each lump mass ($x_1, y_1, x_2, y_2, x_3, y_3$) in terms of the deformation angles (θ_1 , θ_2) as:

$$x_1 = 0 \tag{1}$$

$$y_1 = 0 \tag{2}$$

$$x_2 = L_1 \sin\theta_1 \tag{3}$$

$$y_2 = -L_1 \cos\theta_1 \tag{4}$$

$$x_3 = x_2 + L_2 \sin\theta_2 \tag{5}$$

$$y_3 = y_2 - L_2 \cos\theta_2 \tag{6}$$

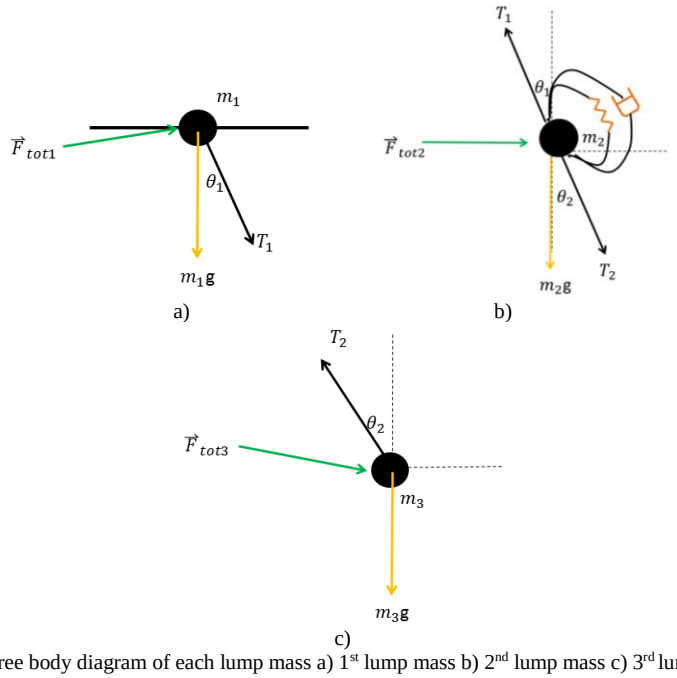

Fig. 2 Free body diagram of each lump mass a) 1st lump mass b) 2nd lump mass c) 3rd lump mass.

The free-body diagram in Fig. 2 shows the net force acting on each mass. The net forces on the 1st mass are zero due to the pivot point. The equation of motion of the 2nd lump mass is represented in the horizontal and vertical components of motion by using the Newton's second law of motion:

$$m_2 a_{x,2} = -T_1 s_1 + T_2 s_2 + F_{x\_tot,2} \tag{7}$$

$$m_2 a_{y,2} = T_1 c_1 - T_2 c_2 - m_2 g + F_{y\_tot,2} \tag{8}$$

Where m_2 is the second lump mass, $F_{x\_tot,2}$ and $F_{y\_tot,2}$ are total force vectors acting on the 2nd lump mass along the x and y direction respectively ($\mathbf{F}_{tot,2} = \mathbf{F}_{\text{int},2} + \mathbf{F}_{ext,2} + \mathbf{F}_{D,2}$), $\mathbf{F}_{\text{int},2}$ is the internal force vector from the summation of rotational damper and spring force vectors ($\mathbf{F}_{\text{int},2} = \mathbf{F}_{spring} + \mathbf{F}_{damper}$), $\mathbf{F}_{ext,2}$ is the external force vector, $\mathbf{F}_{D,2}$ is the air friction, $\mathbf{T}_j$ is the tension force vector generated by the j^{th} rods (j = 1-2), $a_{x,2}$ is acceleration along the x direction of the 2nd lump mass, $s_1 = \sin\theta_1$, $c_1 = \cos\theta_1$, $a_{y,2}$ is acceleration along the y direction of the 2nd lump mass and $s_2 = \sin\theta_2$, $c_2 = \cos\theta_2$. The rotational spring and damper forces are expressed as:

$$\mathbf{F}_{spring} = K_{eq}(\theta_2 - \theta_1)/L_i \tag{9}$$

$$\mathbf{F}_{damper} = C_{eq}(\omega_2 - \omega_1)/L_i \tag{10}$$

Where ω_1 and ω_2 are the angular velocities of L_1 and L_2 respectively, K_{eq} is the equivalent stiffness coefficient and C_{eq} is the equivalent damping coefficient. Despite a high-vacuum chamber, residual air will still exert aerodynamic drag on the MLI due to its low mass and tensile strength [19, 20]:

$$\mathbf{F}_D = -\frac{1}{2}\rho \mathbf{V}_i^2 A C_D \tag{11}$$

Where ρ is the air density, A is the area of the object, $\mathbf{V}_i$ is the velocity of the i^{th} lump mass and C_D is the drag coefficient (C_D of flat plate = 1.9). The equation of motion of the 3rd lump mass is:

$$m_3 a_{x,3} = -T_2 s_2 + F_{x\_tot,3} \tag{12}$$

$$m_3 a_{y,3} = T_2 \, c_2 - m_3 g - F_{y\_tot,3} \tag{13}$$

Then, we substitute Eq.(12) and Eq.(13) into Eq.(7) and Eq.(8):

$$m_2 a_{x,2} = -T_1 s_1 - m_3 a_{x,3} + F_{x\_tot,3} + F_{x\_tot,2} \tag{14}$$

$$m_2 a_{y,2} = T_1 \, c_1 - m_3 a_{y,3} - m_3 g - m_2 g + F_{y\_tot,2} + F_{y\_tot,3} \tag{15}$$

We multiply $\cos\theta_1$ in Eq.(14) and $\sin\theta_1$ in Eq.(15) and rearrange the LHS in term of $T_1 s_1 c_1$:

$$T_1 s_1 c_1 = -c_1 m_2 a_{x,2} - c_1 m_3 a_{x,3} + c_1 (F_{x\_tot,2} + F_{x\_tot,3}) \tag{16}$$

$$T_1 s_1 \, c_1 = s_1 m_2 a_{y,2} + s_1 m_3 a_{y,3} - s_1 (-m_3 g - m_2 g + F_{y\_tot,2} + F_{y\_tot,3}) \tag{17}$$

Then, substituting Eq.(16) into Eq.(17):

$$c_1 (F_{x\_tot,2} + F_{x\_tot,3}) - c_1 m_2 a_{x,2} - c_1 m_3 a_{x,3} = s_1 m_2 a_{y,2} + s_1 m_3 a_{y,3} - s_1 (-m_3 g - m_2 g + F_{y\_tot,2} + F_{y\_tot,3}) \tag{18}$$

In order to find expressions for the angular acceleration of α_1 and α_2 in terms of θ_1, ω_2, θ_2 and ω_2, the second order derivatives of Eq.(3) to Eq.(6) yield:

$$a_{x,2} = -\omega_1^2 L_1 \sin\theta_1 + \omega_1 L_1 \cos\theta_1 \tag{19}$$

$$a_{y,2} = \omega_1^2 L_1 \cos\theta_1 + \alpha_1 L_1 \sin\theta_1 \tag{20}$$

$$a_{x,3} = a_{x,2} - \omega_2^2 L_2 \sin\theta_2 + \alpha_2 L_2 \cos\theta_2 \tag{21}$$

$$a_{y,3} = a_{y,2} + \omega_2^2 L_2 \cos\theta_2 + \alpha_2 L_2 \sin\theta_2 \tag{22}$$

The next step is a substitution of the acceleration from Eq.(19) - Eq.(22) in Eq.(18):

$$\alpha_1 L_1 (m_2 + m_3) + \alpha_2 L_2 m_3 \cos(\theta_2 - \theta_1) - \omega_2^2 L_2 m_3 \sin(\theta_2 - \theta_1) = c_1 (F_{x\_tot,2} + F_{x\_tot,3}) + s_1 (-m_3 g - m_2 g + F_{y\_tot,2} + F_{y\_tot,3}) \tag{23}$$

Following a similar procedure for the 3rd lump mass, we multiply Eq. (12) by $\cos\theta_2$ and Eq.(13) by $\sin\theta_2$ and substitute the acceleration from Eq.(19) - Eq.(22). Finally, the equation for the angular acceleration of the third lump mass will be:

$$\alpha_1 L_1 m_3 \cos(\theta_2 - \theta_1) + \alpha_2 L_2 m_3 + \omega_2^2 L_1 m_3 \sin(\theta_2 - \theta_1) = s_2 (m_3 g + F_{y\_tot,3}) - c_2 F_{x\_tot,3} \tag{24}$$

Eq.(23) and Eq.(24) can be written in matrix form:

$$\begin{bmatrix} C_1 & C_2 \\ C_3 & C_4 \end{bmatrix} \begin{bmatrix} \alpha_1 \\ \alpha_2 \end{bmatrix} = \begin{bmatrix} A_1 \\ A_2 \end{bmatrix} \tag{25}$$

Where:

$C_1 = L_1 (m_2 + m_3)$

$C_2 = m_3 L_2 \cos(\theta_2 - \theta_1)$

$C_3 = m_3 L_2 \cos(\theta_2 - \theta_1)$

$C_4 = m_3 L_2$

$A_1 = \omega_2^2 L_2 m_3 \sin(\theta_2 - \theta_1) + c_1 (F_{x\_tot,2} + F_{x\_tot,3}) + s_1 (F_{y\_tot,2} + F_{y\_tot,3} - (m_2 + m_3) g)$

$A_2 = -\omega_2^2 L_1 m_3 \sin(\theta_2 - \theta_1) + s_2 (m_3 g + F_{x\_tot,3}) - c_2 F_{x\_tot,3}$

By multiplying the left hand side of Eq.(25) by the inverse of the C matrix. We can define the angular acceleration vector as:

$$\begin{bmatrix} \alpha_1 \\ \alpha_2 \end{bmatrix} = \begin{bmatrix} C_1 & C_2 \\ C_3 & C_4 \end{bmatrix}^{-1} \begin{bmatrix} A_1 \\ A_2 \end{bmatrix} \tag{26}$$

The numerical integrator used to solve the dynamics of the multibody model equations is the Runge-Kutta method (ODE45) in MATLAB® : RelTol: 1.0×10^{-8}, AbsTol: 1.0×10^{-8}. It requires to convert the 2nd order equations into the 1st order equations. Then, the new system is written as:

$$\begin{bmatrix} \dot{\theta}_1 \\ \dot{\theta}_1 \\ \dot{\omega}_1 \\ \dot{\omega}_2 \end{bmatrix} = \begin{bmatrix} \omega_1 \\ \omega_2 \\ \alpha_1 \\ \alpha_2 \end{bmatrix} \tag{27}$$

All simulations in this paper are performed on a PC with Intel core i7@ 1.80 GHz and 8GB RAM.

3. MATERIAL PROPERTIES

Three samples [17, 18] are used in this paper: PET® 1 mil, Kapton® 1 mil and PET® 5 mils. PET® is aluminized on both sides while Kapton® is aluminized only on one side. All samples have the same width (5 cm) and length (20 cm) and their physical characteristics and properties are shown in Table 1.

Table 1 Properties of the PET and Kapton samples [17, 18]

Sample	Thickness mil (μm)	Mass (mg)	Density (kg/ m^3)	Young's Modulus (N/m^2)	*Cs*, *Cd*, *Ca*
PET 1mil	1(25.4)	0.3530	1,390	$8.81x10^9$	0.60 0.26 0.14
PET 5 mil	5(127)	1.7653	1,390	$8.81x10^9$	0.60 0.26 0.14
Kapton 1 mil	1(25.4)	0.3606	1,420	$2.50x10^9$	0.60 0.26 0.14

The two experiments in this paper (free motion and radiation pressure experiments) are performed in a vacuum chamber (size: 30×30×28.7 cm^3) in order to replicate the space environment and both experimental setup will be described in the next section.

4. FREE MOTION EXPERIMENT

This experiment aims to find the damping characteristics and mode of vibration of each sample. The experimental results will be compared with the results from the analytic method and multibody simulations.

4.1 Experimental setup

The setup for the free motion test is shown in Fig. 3. The sample is attached by means of a stand and held in place by an electromagnetic latch. The camera (Canon IXUS 110 IS, 30fps) is set in front of the mirror window. Before starting the experiment, the vacuum chamber is pumped down to 1×10^{-4} mbar. The electromagnetic latch is then turned off, releasing the sample, which swings freely and this motion is recorded by the camera. The data are used for the object tracking process to allow measurement of the amplitude decay through a Fast Fourier Transform (FFT) to identify the natural frequencies of the different MLI samples.

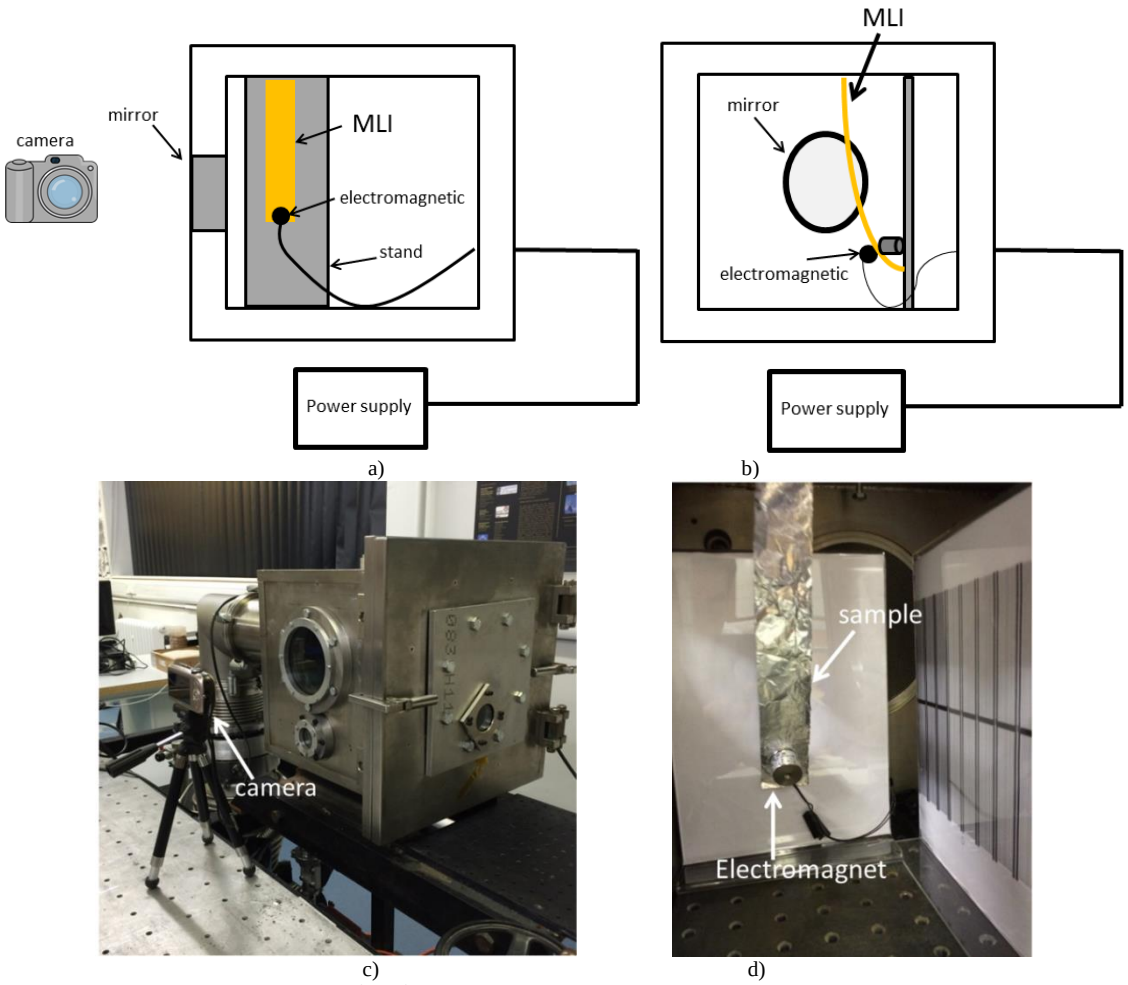

Fig. 3 Schematic drawing and experimental setup of the free motion experiment. a) side view b) back view c) experimental set up d) inside the vacuum chamber.

4.2 Object tracking

In order to measure the motion of the MLI sample inside the vacuum chamber during the experiment, object motion tracking, through a recorded video, is used. This is achieved by measurement of the movement of a red point, representing the lump mass of the multibody model. There are five major steps in this process:

1. The motion of the sample is converted to an image sequence (Fig. 4(a)).
2. The three red pixels are then extracted and separated from the blue and green pixels (Fig. 4(b)).
3. In the object recognition and representation step (Fig. 4(c)), the extracted red pixels are converted to white in a binary image.
4. Next, this will then allow to process a representation of each recognized tracked object.
5. The last step, Kalman filter tracking, uses a Kalman algorithm [21-23] to estimate an observable state, which is updated at each time step through a linear state update, and plots the tracking blue rectangle around the object's movement at each time step (Fig. 4(d)).

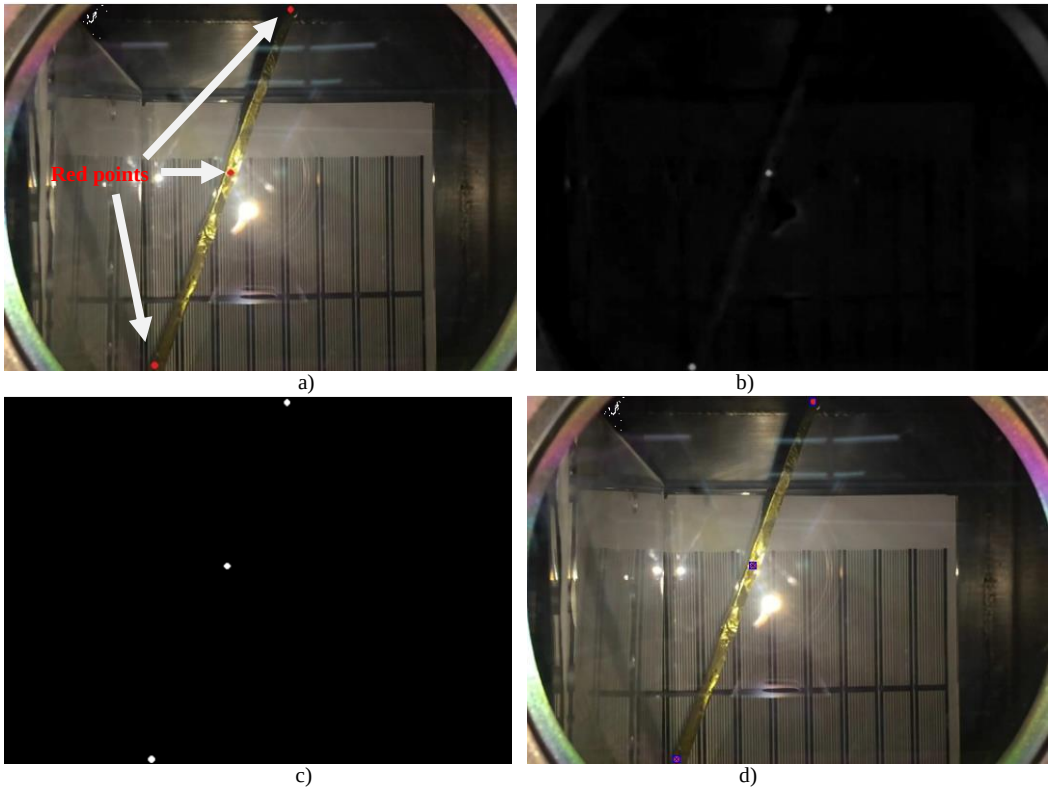

Fig. 4 Object tracking process a) an extracted image from a video record b) Extracting the red pixels from a picture c) Converting a grayscale image into a binary image d) Blue mark on the red three points on an image.

4.2.1 Kalman filter

The Kalman filter [24] is an algorithm that uses a series of measurements observed over time to predict a future state and uses available measurements to correct this prediction. For visual object tracking, Kalman filtering is usually achieved by representing the uncertainty via a Gaussian function, to balance the effects of tracking results from observation and prediction. In this experiment, the state measurements of the free motion experiment are represented by the positions of three red points. The Kalman filter algorithm has, two steps: prediction and update.

4.2.1.1 Prediction

The prediction step makes use of the state estimate from the previous time step to produce an estimate of the state at the current time step.

1) State prediction, $\hat{x}_{i+1}^{-}$: a Kalman filter makes a prediction of the state at i +1 defined by:

$$\hat{x}_{i+1}^{-} = \Phi_s \hat{x}_i \tag{28}$$

Where Φ_s is the state transition matrix and $\hat{x}_i$ is the current state vector.

2) State covariance prediction: a Kalman filter estimates the error covariance P_{i+1}^{-} forward as:

$$P_{i+1}^{-} = \Phi_s P_i \Phi_s^T + Q \tag{29}$$

Where Q is the process noise covariance and P_i is the error covariance matrix.

4.2.1.2 Measurement update

After predicting the state and its error covariance at time i +1 the process then continues as:

1) Kalman Gain: the Kalman filter computes a Kalman gain K_{i+1} used to correct the state estimates $\bar{X}_{i+1}$:

$$K_{i+1} = P_{i+1}^{-} H_{i+1}^{T} (H_{i+1} P_{i+1}^{-} H_{i+1}^{T} + R)^{-1} \tag{30}$$

Where H_{i+1} is a matrix that converts the state space into a measurement space at i +1 and R is a measurement noise covariance.

2) Update Estimate with measurement $\hat{x}_{i+1}^{-}$: the Kalman gain and measurement from the new time step, are then used to update the state estimate as;.

$$\hat{x}_{i+1} = \hat{x}_{i+1}^{-} + K_{i+1}[Z_{i+1} - H_{i+1}\hat{x}_{i+1}^{-}] \tag{31}$$

Where Z_{i+1} is the measurement vector.

3) Update error covariance estimate (P_{i+1}): the final step of the Kalman filter's iteration is the update of the error covariance P_{i+1}^{-} to P_{i+1}.

$$P_{i+1} = [I - K_{i+1} H_{i+1}] P_{i+1}^{-} \tag{32}$$

Where I is the identity matrix.

4.3 Underdamped free vibration

The free motion of the membrane is slowly damped due to friction present in the hinge and residual atmosphere in the vacuum chamber. The amplitude of the oscillation decrease decay over time and the damped vibration period (τ_d) is defined as:

$$\tau_d = \frac{2\pi}{\omega_d} \tag{33}$$

Where ω_d is the damped natural frequency: $\omega_d = \sqrt{1-\xi^2}\,\omega_n$ and ω_n is the natural frequency of the system.

The amplitude response in the time domain can be transformed into the frequency domain by using FFT in order to estimate the damping ratio of a sample. The half-power bandwidth from the frequency response is a very useful tool for computing the damping ratios for multi freedom systems as:

$$\xi = \frac{(\omega_2 - \omega_1)}{2\omega_n} \tag{34}$$

From the amplitude decay and frequency response in, we can find an equivalent stiffness constant (K_{eq}), and equivalent damping coefficient (C_{eq}). They are defined as:

$$K_{eq} = \omega_n^2 M \tag{35}$$

and

$$C_{eq} = 2M\omega_n\xi \tag{36}$$

Where M is the total mass of the membrane. We can now measure the damping ratio of the material by observing the amplitude decay of the displacement and computing the natural frequency from the frequency response.

4.3.1 Normal modes

Based on an unforced, damped two-degree-of-freedom mass-spring-damper system $[\theta_1, \theta_2]$, the generic differential equation is written as following:

$$[M]\boldsymbol{\alpha}+[C]\boldsymbol{\omega}+[K]\boldsymbol{\theta}=0 \tag{37}$$

Where $[M]$ is mass matrix, $[C]$ is the damping coefficient matrix, $[K]$ is the stiffness matrix, $\boldsymbol{\alpha}$ is the angular acceleration vector, $\boldsymbol{\omega}$ is the angular velocity vector and $\boldsymbol{\theta}$ is the angular displacement vector. In order to analyse the normal modes of oscillation of the multibody model, we reduce Eq.(37) to a standard eigenvalue form by removing the damping matrix. The new equation can be written as:

$$[M]\boldsymbol{\alpha}+[K]\boldsymbol{\theta}=0 \tag{38}$$

And the general solution has the form: $\theta_{1,2}(t)=A_{1,2}e^{j\omega t}$. Therefore, we can find the normal modes as:

$$\det([K]-\omega^2[M])=0 \tag{39}$$

The natural frequencies [25], which are the eigenvalues (ω^2) of the multibody model, are determined by solving Eq.(39) as the solution of the quadratic equation.

$$\omega_{\pm}^2=\frac{k_1k_4+k_2k_5\pm\sqrt{(k_1k_4-k_2k_5)^2+2k_1k_5k_6^2}}{2\left(k_2k_4-k_6^2\right)} \tag{40}$$

where

$k_1=g(m_{rod,2}L_1+m_{rod,1}L_1/2)$

$k_2=I_1+m_{rod,1}L_1^2+m_{rod,1}(L_1/2)^2$

$k_4=m_{rod,2}(L_1/2_1)^2+I_2$

$k_5=-m_{rod,2}g(L_1/2)$

$k_6=-L_1m_{rod,2}(L_1/2)$

I_1 and I_2 are the moments of inertia of rigid rod

From Eq.(40), we can find the normal modes of the oscillation. The ratios of the amplitude A_1 and A_2 of two coordinates are expressed as:

$$\left(\frac{A_1}{A_2}\right)_{\pm}=\frac{-k_5k_6}{\omega_{\pm}^2\left(k_2k_4-k_6^2\right)-k_1k_4} \tag{41}$$

The 1st mode ($(A_1/A_2)_+ > 0$) represents both rigid rods oscillating in the same direction (in-phase in Fig. 5(a)). The 2nd mode ($(A_1/A_2)_- < 0$) implies that the rigid rods move in opposite directions (out of phase in Fig. 5(b)). The analytic method to determine natural frequency, called "*normal mode*", will be compared with modal analysis performed using ANSYS® and the experimental results obtained during free motion experiment.

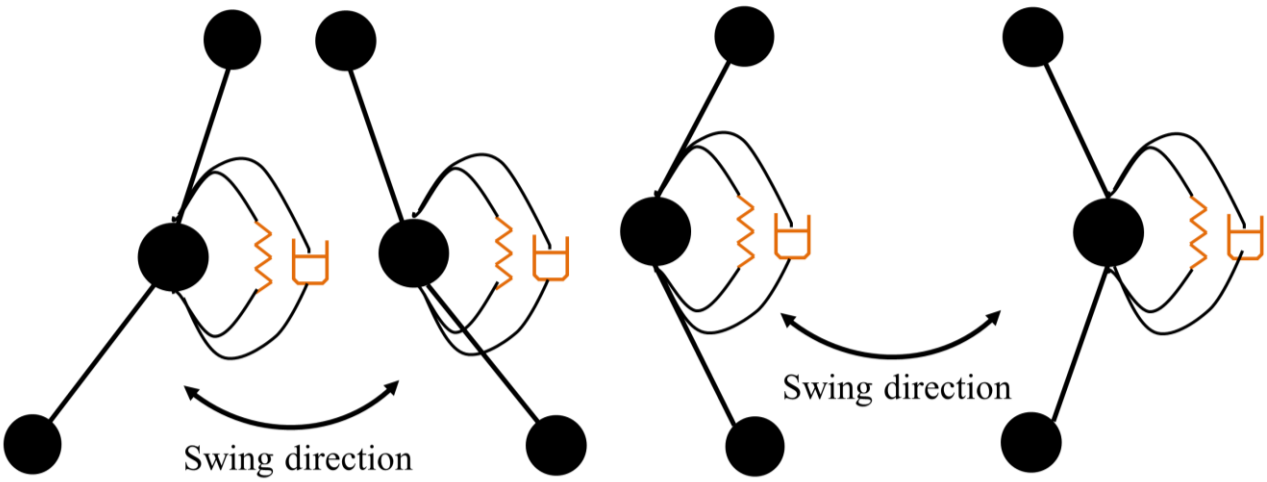

a) b)

Fig. 5 Two normal modes of multibody model a) 1st mode b) 2nd mode.

4.4 Experimental results

Fig. 6 shows the angular motion of the Kapton 1 mil MLI element under normal atmospheric conditions. The result shows that air friction plays a major role in supressing the motion of the MLI element, with the oscillations stopped after just 3 seconds. The object tracking detections of the free fall motion of PET 1 mil, Kapton 1 mil and PET 5 mils in vacuum environment are shown as in Fig. 7, Fig. 8 and Fig. 9 respectively. The motion of the lump masses are denoted by a blue rectangle.

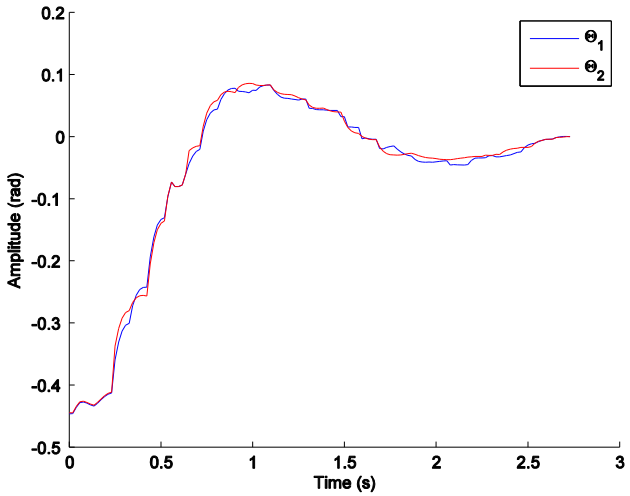

Fig. 6 Free vibration response of Kapton 1 mil in normal atmosphere.

a) b) c)

Fig. 7 Detection of red components of PET 1 mil.

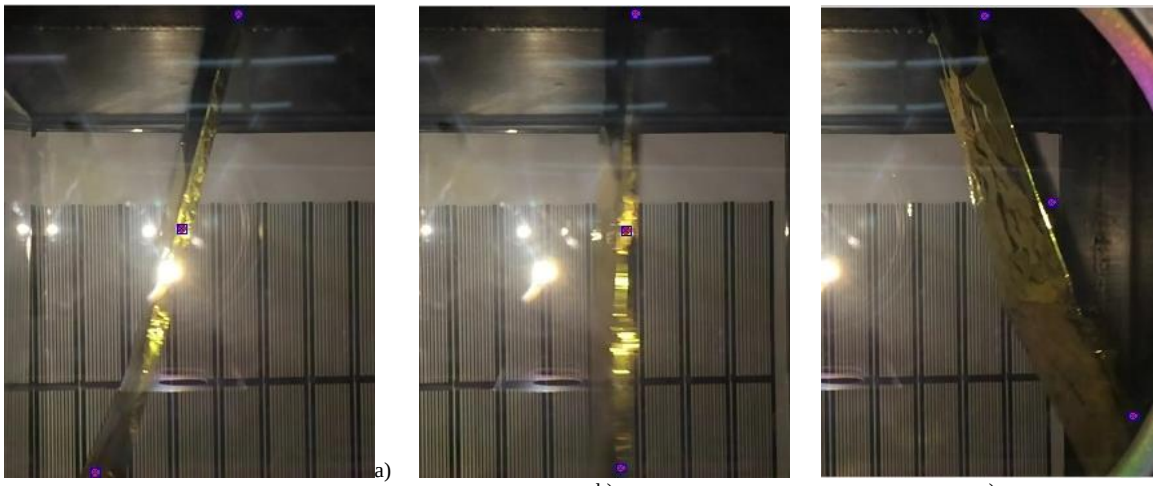

a) b) c)

Fig. 8 Detection of red components of Kapton 1 mil.

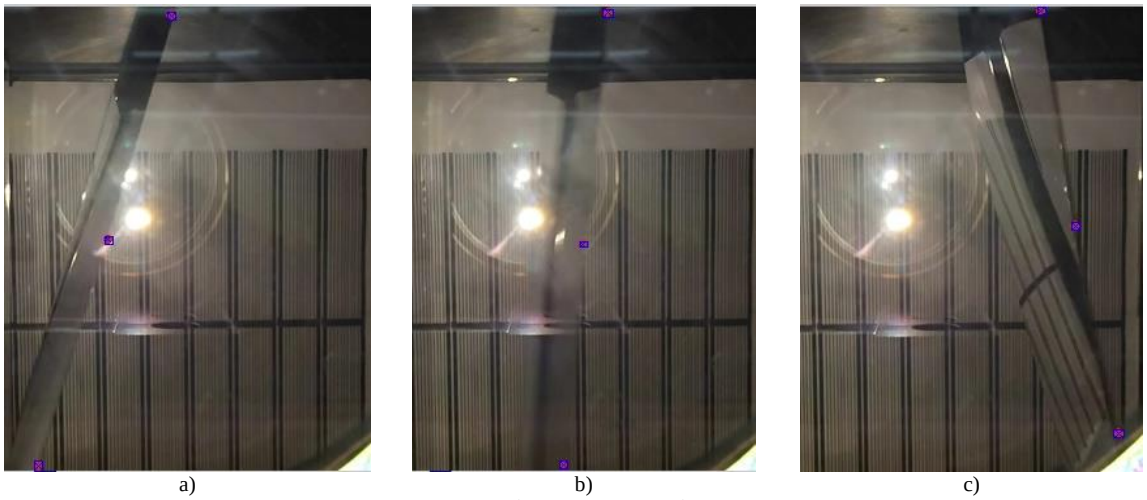

a) b) c)

Fig. 9 Detection of red components of PET 5 mils.

Fig. 10 shows the free vibration of the deformation angles θ_1 and θ_2 in the time and frequency domains for each MLI sample. The settling times of the PET 1 mil, Kapton 1 mil and PET 5 mils are 12.41, 12.52 and 24.30 seconds respectively. It is obvious that amplitude, settling time and natural frequency of a sample depend on its material properties. The bigger mass will affect the higher gravitational potential energy. With more energy, the bigger mass will

swing faster. The bending of all samples measured by the absolute difference of θ_1 and θ_2 decreases over time. From these results, we can compute the damping ratio (ξ) from Eq.(34). The equivalent rotational spring and damping coefficients on the 2nd lump mass can be calculated with Eq.(35) and Eq.(36) respectively. Table 2 shows the damping ratio, stiffness and damping coefficients obtained from the experimental data. We will use the values in Table 2 to investigate the amplitude decays and natural frequencies of the multibody model.

Table 2 Damping ratio, stiffness and damping coefficients of MLI sample from experimental results.

Sample	ξ	K_{eq} ($N \cdot m/rad$)	C_{eq} ($N \cdot m \cdot s/rad$)
PET 1 mil	0.0409	0.0258	2.467E-04
Kapton 1mil	0.0441	0.0251	2.652E-04
PET 5 mils	0.0145	0.1162	4.153E-04

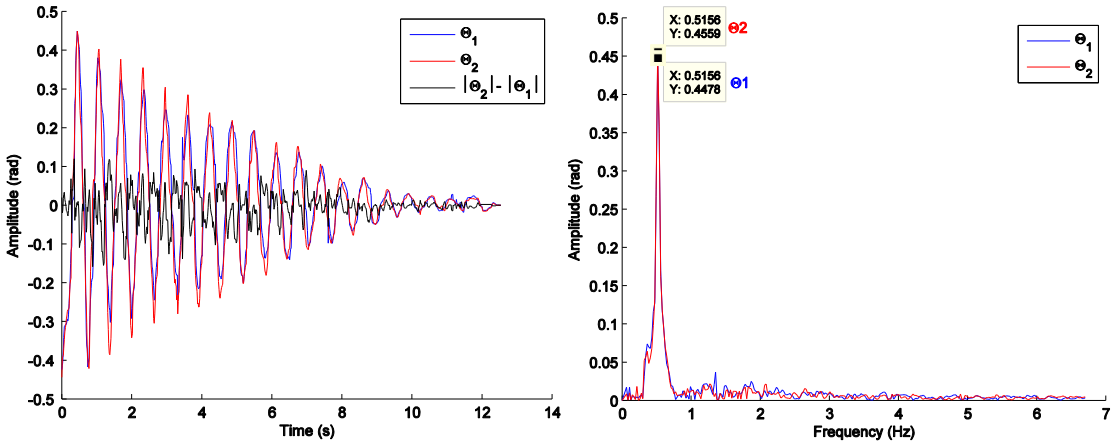

a)

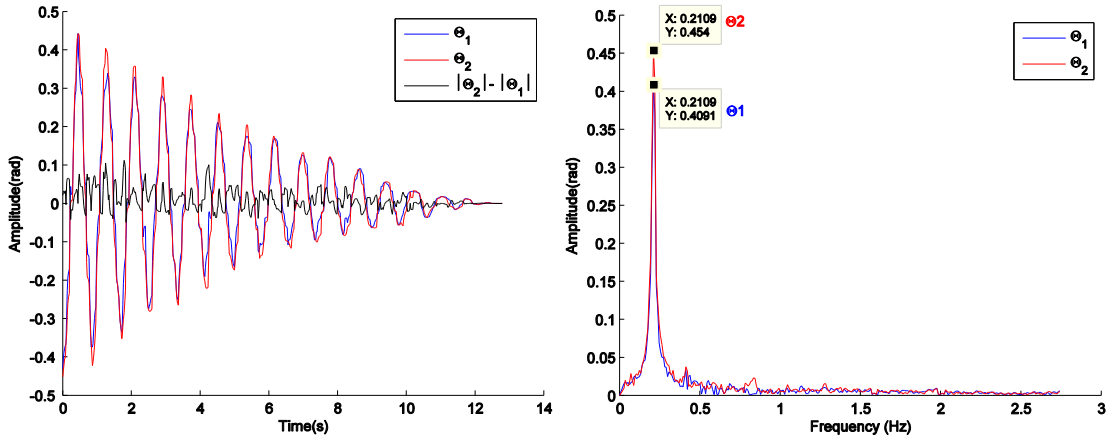

b)

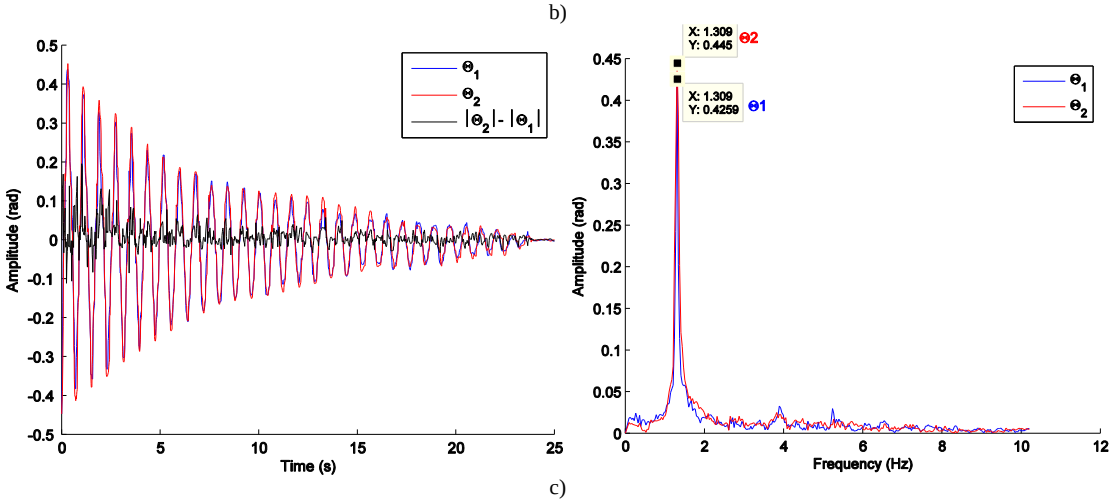

c)

Fig. 10 Free vibration response of the free motion experiment in time and frequency domains a) PET 1 mil b) Kapton 1 mil c) PET 5 mils.

The free motion simulation of the numerical multibody model of Kapton 1 mil is shown in Fig. 11. In the result summary of all samples, the settling times of the PET 1 mil, Kapton 1 mil and PET 5 mils are shown in Fig. 12 and are 24.30, 25.10 and 40.10 seconds respectively. As shown in the experimental results, Kapton 1 mil takes the shortest time to stabilise while PET 5 mils takes the longest. The results are coherent with the damping ratios (ξ), as Kapton 1 mil and PET 5 mils have the highest and lowest damping coefficient (C_{eq}) respectively. Comparing the experimental results with the numerical simulations, we can see that the motion appears to match well for the initial 2-3 cycles but then the settling time for the numerical results are approximately double that of the experimental results. This is caused by the presence of dissipative forces at the hinge inside the vacuum chamber that are not modelled in our system dynamics.

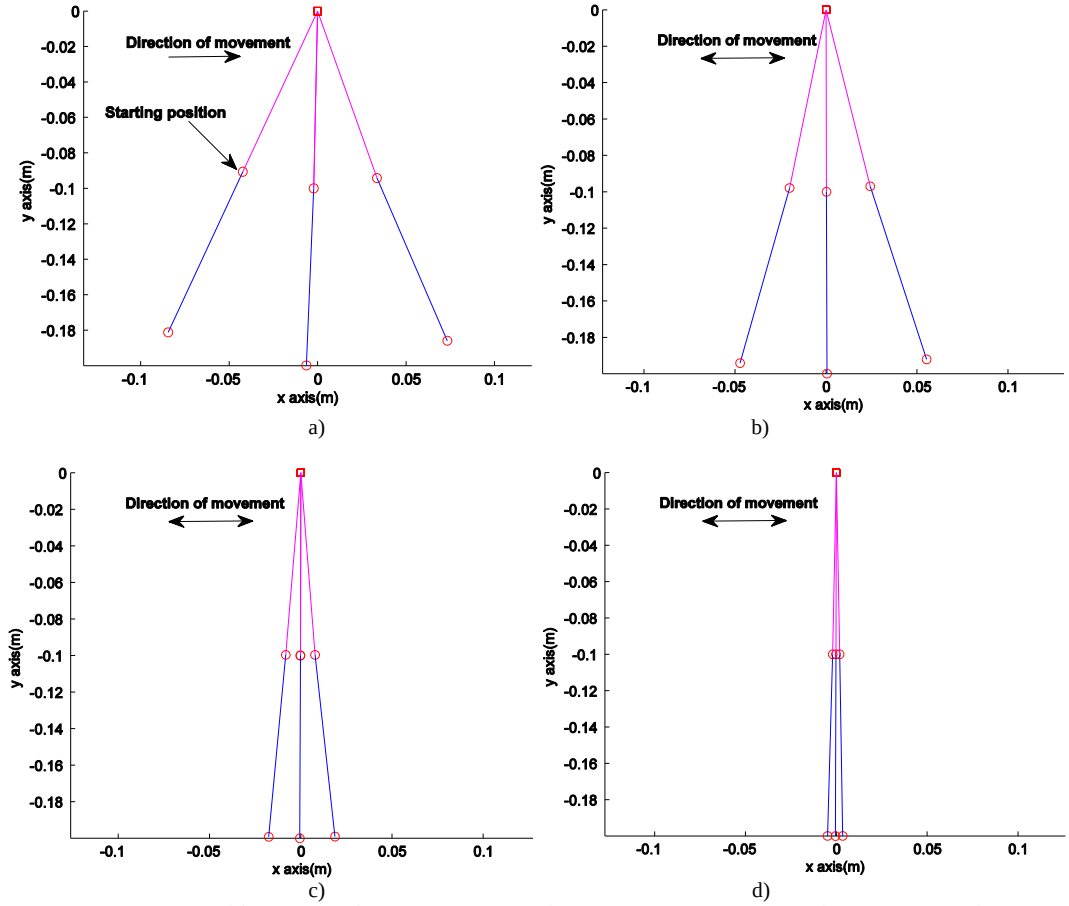

Fig. 11 The simulation example of free motion of multibody dynamics for Kapton a) 0–0.5 second b) after 3 seconds c) after 10 seconds d) after 20 seconds.

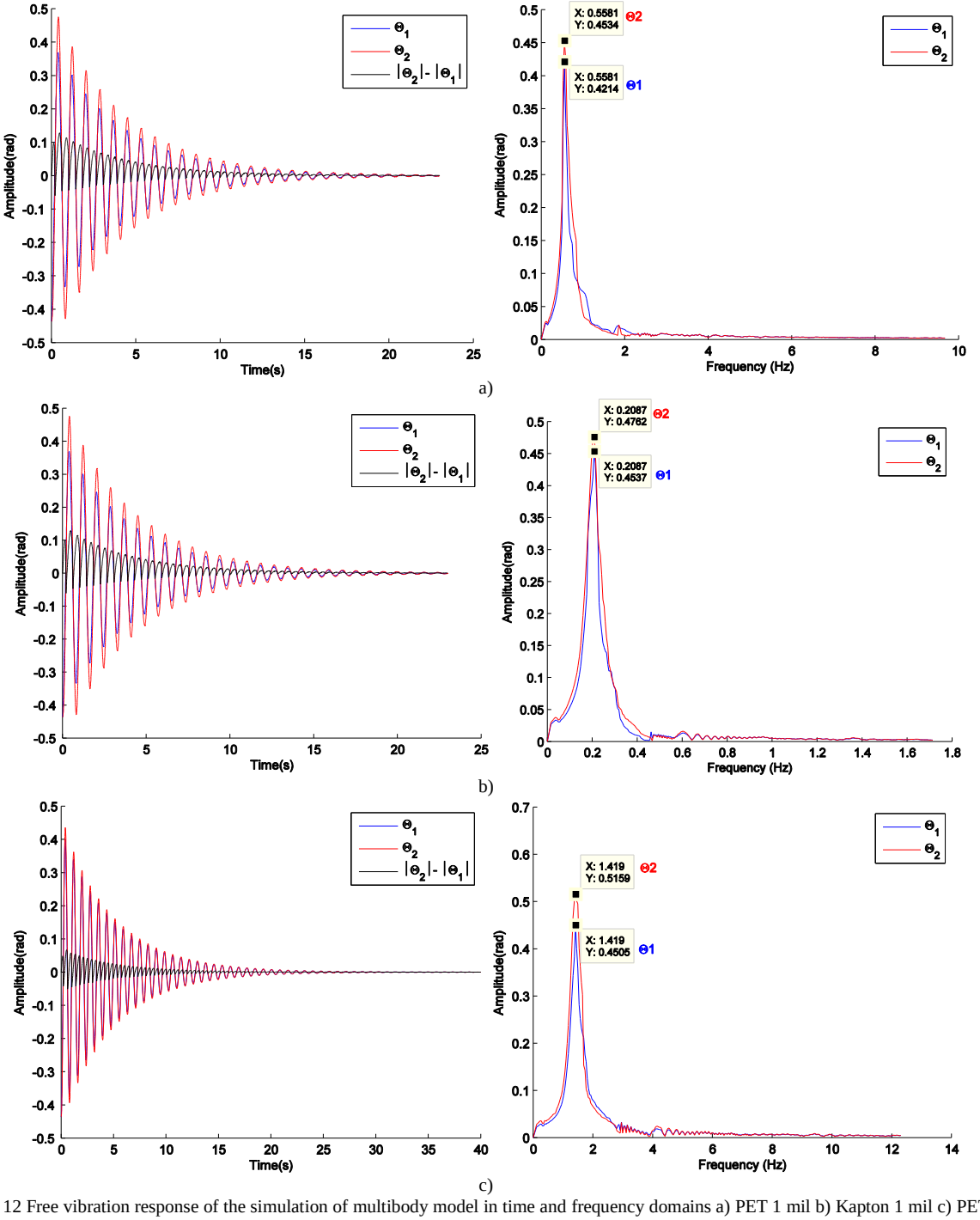

Fig. 12 Free vibration response of the simulation of multibody model in time and frequency domains a) PET 1 mil b) Kapton 1 mil c) PET 5 mils.

The natural frequencies of the PET 1 mil, Kapton 1 mil and PET 5 mils from the experimental results in Fig. 10 are 0.5156, 0.2109 and 1.3090 Hz which match well with the results obtained through the numerical simulations in Fig. 12 (0.5581, 0.2087 and 1.4190 Hz respectively). The numerical results appear to have a smoother profile than the experimental results as some configurations (twisting form e.g. Fig. 8 and Fig. 9) occur during the experiment. We now analyse the phase of both θ_1 and θ_2 in order to investigate the normal mode of the oscillation response. We can see from Fig. 10 and Fig. 12 that in both numerical and experimental results, the amplitudes of all samples are in-phase throughout the motion. These results therefore imply that the natural frequency of all samples is in the 1st mode as shown in Fig. 5(a).

For further comparison, FEA simulations performed with commercial software (ANSYS®) are performed in order to validate the experimental results and multibody model. The numerical results of the modal analysis of the 1st and 2nd modes of all samples with ANSYS® in Fig. 13 are similar to the normal mode of the multibody model in Fig. 5(a). The summary of the natural frequency values, obtained through experimental results, numerical multibody model simulations, normal mode through Eq.(40) and FEA are shown in Table 3. We can see that the natural frequency for all samples appears to be very similar, thus we believe this experimental method can help to define the damping characteristics of a sample and the multibody model is able to predict the free vibration of a sample.

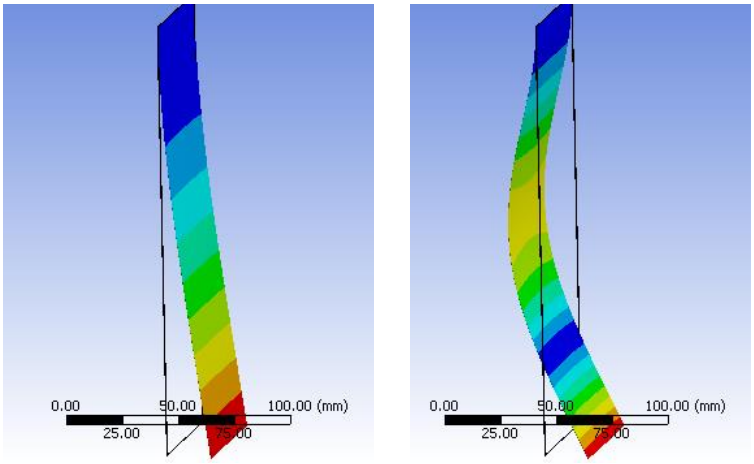

a) b)

Fig. 13 Mode shape and the natural frequencies results of PET 1 mil from FEA (ANSYS®): Natural modes a) the 1st mode b) the 2nd mode.

Table 3 Natural frequency comparison.

Material	Natural Frequency (Hz)					
	Free vibration simulation (MATLAB®)	Free vibration method (Experiment)	Normal mode (Theory)		Free vibration method (ANSYS®)	
	f_1	f_1	f_1	f_2	f_1	f_2
PET 1 mil	0.5581	0.5156	0.5265	1.3474	0.5350	1.3815
Kapton 1mil	0.2087	0.2109	0.2299	0.6147	0.2095	0.6270
PET 5 mils	1.4190	1.3090	1.3480	8.1566	1.3338	8.3209

Where f_1 and f_2 are the 1st and 2nd modes of natural frequency respectively.

5. RADIATION PRESSURE EXPERIMENT

The second experiment aims to measure the displacement of the free end of a membrane by exposing it to the radiation pressure from a high power spotlight. The experimental results will then be compared with the numerical results obtained from the analytic solution of both multibody dynamics and FEA simulations (through commercial package ANSYS®).

5.1 Experimental setup

For the experimental set up illustrated in Fig. 14, a high power spotlight is (theatre spot 2000 Antihalo bk [26]) beamed onto the sample. A dimmer (strairville ns 2003 dimmer resist) allows the spotlight irradiance to be adjusted in order to study the relationship between irradiance and sample displacement. A high resolution laser measurement system optoNCDT 1700-2LL [27], (resolution: 0.1µm and measuring range 2 mm) was used to measure the displacement at the bottom of sample (the 3rd lump mass) as shown in Fig. 14(c). The RS422 converter [27], which converts serial data from

the sensor to a USB port, is installed to interface the sensor with a laptop. The experiment was repeated five times (100 measurements/time) on each sample and the average of the five measurements are used here to critically evaluate the results.

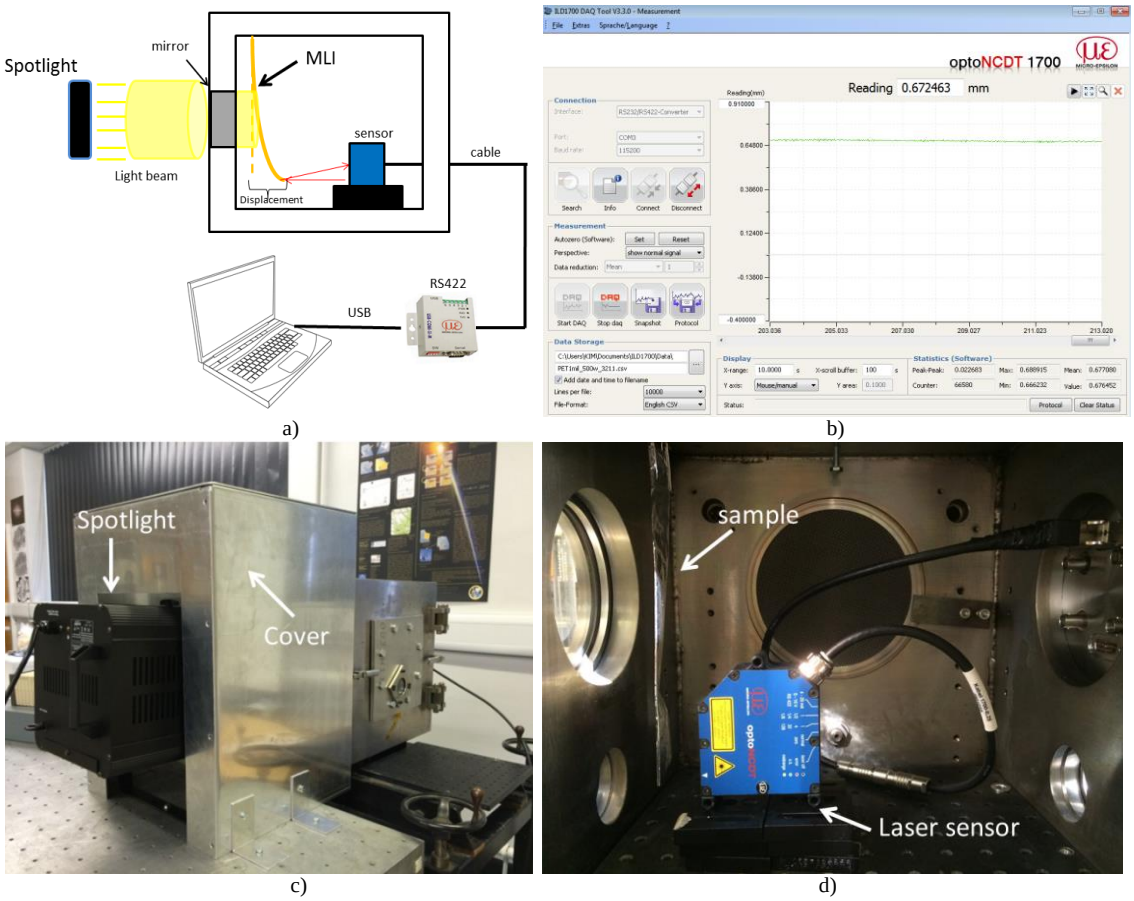

Fig. 14 Schematic drawing and experimental set up of a radiation pressure experimental setup a) schematic on side view b) program GUI c) external view of the experiment d) inside view of the vacuum chamber.

5.2 Radiation pressure force of the spotlight

In order to investigate the effect of solar radiation pressure on a sample, the high power spotlight was assumed to emit a collimated beam by using a parabolic mirror [21] as shown in Fig. 15. The estimation of the radiation pressure is given by:

$$I_{rad} = \frac{2P\varepsilon}{4\pi d^2} \tag{42}$$

Where I_{rad} is radiation flux, P is the power of the spotlight, d is the distance of the light source from the membrane and ε is the transmissivity efficiency of the clear glass window of the vacuum chamber, which is approximated as perfect (ε =1).

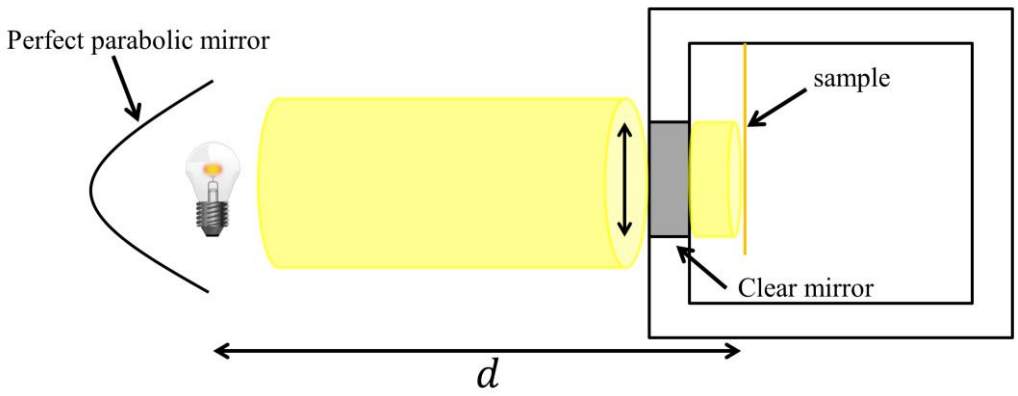

Fig. 15 Schematic drawing of spotlight exposure.

In this experiment, we need to account for the specular and diffuse reflection properties of the MLI. Therefore, the solar radiation force [28] can be calculated as:

$$\mathbf{F}_{rad} = \frac{I_{rad}}{C} A_{\exp} \cos(\theta_{inc}) \left(2\left(\frac{C_{Rd}}{3} + C_{Rs} \cos(\theta_{inc}) \right) \hat{N} + (1 - C_{Rs}) \hat{S} \right) \tag{43}$$

Where $A_{\exp}$ is exposed area of sample, c is the speed of light (299,792,458 m/s), C_{Rd} , C_{Rs} and C_{Ra} are the coefficients of diffuse, specular and absorbed reflectivity respectively. The relationship between C_{Rs} , C_{Ra} and C_{Rd} is $1 = C_{Rs} + C_{Ra} + C_{Rd}$, $\hat{N}$ is the normal unit vector of membrane, $\hat{S}$ is the spotlight incidence unit vector. In this experiment, the spotlight operates along the x axis direction and the incident angle (θ_{inc}) is perpendicular to the membrane. Then, Eq. (43) defines the external force acting on the MLI element. In order to apply the radiation pressure force on the multibody model, the exposed areas in Fig. 16 is separated in two parts and each force is divided on each lump mass. In case of the FEM model, the exposed areas in Fig. 17 are defined by selecting the required element nodes.

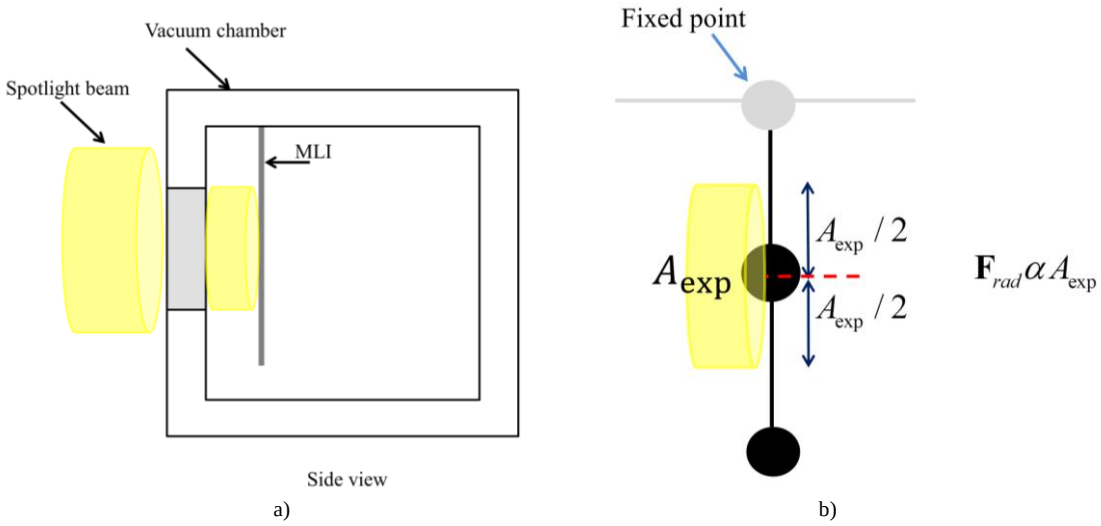

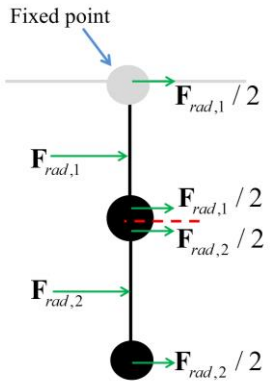

Where : $\mathbf{F}_{rad,1} = \frac{A_{exp}}{2} P, \mathbf{F}_{rad,2} = \frac{A_{exp}}{2} P$

$\mathbf{F}_{rad,i}$: Radiation pressure force on i^{th} plane (i = 1 and 2)

$\boldsymbol{P}$: radiation pressure

A_{exp} : Exposed area

c)

Fig. 16 Exposure of spotlight on a specimen a) real specimen b) multibody model c) radiation pressure force on each lump mass.

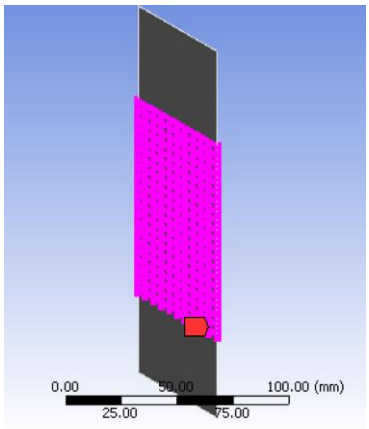

Fig. 17 Schematic drawing of spotlight exposure of the FEM model.

5.3 Experimental results

To determine the motion of the MLI samples subject to external forces, we illuminate the samples with a high power spotlight. The spotlight is calibrated at four different power values (500, 1000, 1500 and 2000 W) and each experiment (coupling of MLI sample and power intensity) is run five times with the results then averaged. Fig. 14 shows that the numerical and FEA results align well with the experimental results. All results show very small displacements (in the order of micrometres). The displacement of the numerical result is lower than that for FEA and experiment, however all results show small nonlinear behaviour for all membrane types.

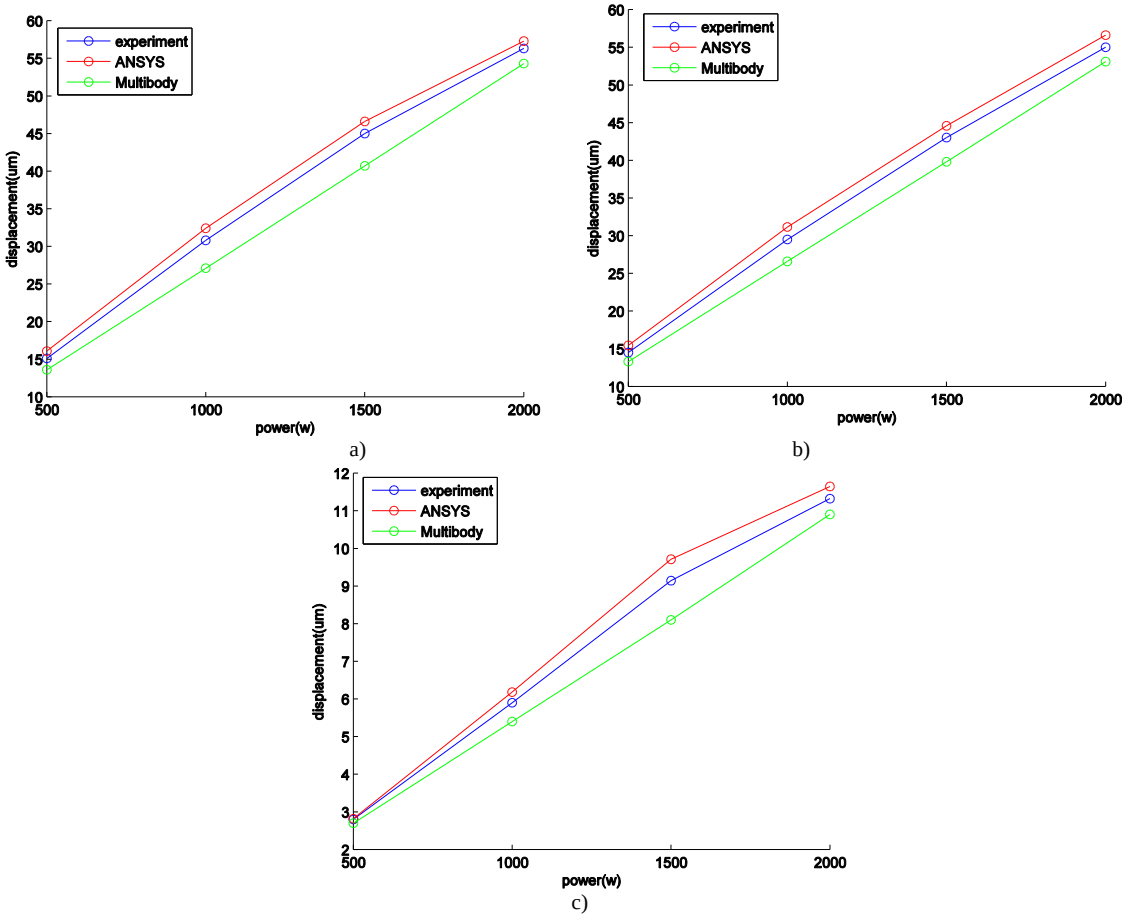

Fig. 18 Comparison of displacement results of radiation pressure experiment, FEA and multibody dynamics a) PET 1 mil b) Kapton 1 mil c) PET 5 mils.

Table 4 shows the relative error (Δ) of the displacement of the numerical and FEA compared to the experimental results. The relative error of the numerical model is the largest (12.01%) at 1000W while the relative error of FEA has the maximum relative error at 500W for both PET 1 mil (6.46%) and Kapton 1 mil (6.48%) but the relative minimum error is PET 5 mils (0.70%). The relative error of both numerical and FEA of all membrane types at 2000W is less than the relative error at 1000W and 1500W for all cases but not that of the relative error of FEA (PET 5 mils, $\Delta = 0.70\%$) at 500W. To summarize, the relative error range of the numerical model is 3.45-12.01% while the relative error range of FEA is 0.70-6.48%. We can notice that when increasing the high power of spotlight, the relative error trends of FEA of all experiments are lower than those of multibody model. This is because FEA is able to handle a truly arbitrary shape, nonlinear material and nonlinear large-deformation. However, when the deformation motion is coupled with the attitude and orbital dynamics propagation, the computational cost of using such a software becomes unduly large. With this in

mind, the numerical model appears to be more than adequate to provide a fairly accurate first estimate of the motion of an orbiting MLI element subject to environmental perturbations when comparing with the traditional model [16].

Table 4 The relative error of the analytic simulation (Multibody model and FEA) compared to the measured displacement.

Sample	Method	Δ (%error)			
		500(w)	1000(w)	1500(w)	2000(w)
PET 1 mil	Multibody	-9.93	-12.01	-8.13	-3.55
	FEA	6.46	5.19	5.20	1.73
Kapton 1mil	Multibody	-8.28	-9.83	-7.48	-3.45
	FEA	6.48	5.59	5.62	2.90
PET 5 mils	Multibody	-3.57	-8.49	-11.40	-3.71
	FEA	0.70	4.75	6.20	2.88

In order to improve the accuracy of the multibody model, Fig. 19 shows the comparison in the displacement results of the multibody model for each sample by varying the reflection properties of the samples with the results obtained from the FEA. The displacement results by varying power 500 – 1,500 W of both PET 1 mil, Kapton 1 mil and PET 5 mils with reflection property: C_s = 1.0 and C_d = 0 (perfect specular reflection, green line) show the highest improvement when compared to other reflection properties. At 1,500 W of both PET 1 mil and Kapton 1 mil, the displacement results are very close to the results of FEA as shown in Fig. 19(a) and Fig. 19(b) respectively. For 2,000 W, and reflection property: C_s = 0.6 and C_d = 0.4 of both PET 1 mil and Kapton 1 mil (black line) appears to provide higher accuracy, while with reflection properties of C_s = 0.8 and C_d = 0.2. PET 5 mils provides a better approximation than in the case of the perfect specular reflection. This investigation suggests that the finite element analysis software handles a nonlinear problem better than the numerical model. In this investigation, the perfect specular reflection properties (C_s = 1.0, C_d = 0) is probably the most suitable assumption for all samples because the solar radiation pressure (4.51×10^{-6} N/m^2) is converted to be 1,570 W by means of Eq.(42). The reason is that the more highly specular reflection will reflect the more same incident angles because the normal line along the surface is more same. These results are in the increment of radiation force. It can imply that we can improve the accuracy of the multibody model by compensating the reflection properties.

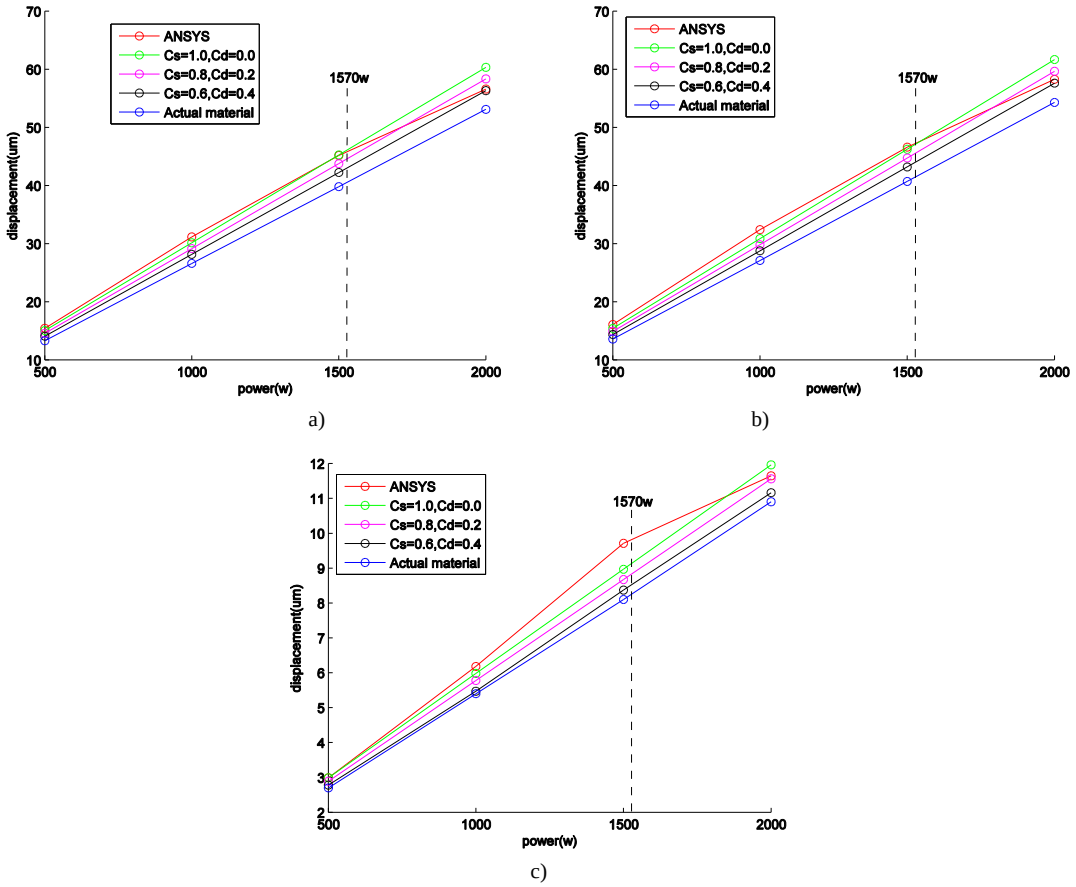

Fig. 19 Comparison of displacement results of FEA with multibody model by varying reflection properties a) PET 1 mil b) Kapton 1 mil c) PET 5 mils.

6. CONCLUSIONS

This paper presents two experiments used to validate a multibody model of flexible HAMR orbital debris. The first experiment (free motion experiment) is carried out to measure the damping characteristics of the membranes and their fundamental natural frequency. The second experiment is performed to simulate the effects of solar radiation pressure on a membrane by exposing it to the radiation pressure force of a high power spotlight. Both experimental results and the simulations of multibody model are validated by analytic theory and finite element analysis (FEA).

The free motion experiment is effective in measuring the damping characteristic of a thin and low strength membrane. Through this method we are able to determine the damping characteristics of each sample. The natural frequencies results obtained by multibody model are in good agreement with both experimental and analytic methods (the natural frequency theory and FEA). The multibody model can thus be an effective simple model for this debris type if we can determine their internal damping characteristics. The experimental results of all samples however show that their amplitude decays reach to steady state faster than the results of the multibody model due to the presence of residual air in the vacuum chamber and hinge friction.

The results of the radiation pressure experiment of the multibody model appear to be in good agreement with both the experimental and FEA results. The relative errors of FEA are better than those obtained from the multibody model due to FEA being able to better tackle systems with higher degree of freedom. In case of orbital propagation, the use of FEA will however result in exorbitant computational costs and hence the multibody model provides a cheaper alternative to obtain a first order approximation of the orbital dynamics of this debris type when compared with traditional models. Increased accuracy of multibody model can be however improved by compensating the reflection properties of a sample.

Future work aims to investigate the thermal expansion of the MLI membrane, which may be responsible for part of the material deformation due to thermal bending. The validation of the radiation pressure force from the spotlight can be validated by means of a light detector to measure the actual power of the spotlight on a membrane and comparing it with the calculation of the radiation exposure equation. The accuracy of the multibody model can be improved by increasing the number of lump masses and allowing for additional folding directions (e.g. 3D deformation).

Acknowledgements

This work was funded by Ministry of Science and Technology of the Thai government and the European Office of Aerospace Research and Development (project award FA8655-13-1-3028).

References

1. Schildknecht, T., et al. *Color photometry and light curve observations of space debris in GEO*. in *Proceedings of Advanced Maui Optical and Space Surveillance Technologies Conference*. 2008. Maui Hawaii.
2. Früh, C. and T. Schildknecht, *Variation of Area-to-Mass-Ratio of HAMR Space Debris objects.* Monthly Notices of the Royal Astronomical Society, 2011. 419(4): p. 3521-3528.
3. Schildknecht, T., R. Musci, and T. Flohrer, *Properties of the high area-to-mass ratio space debris population at high altitudes.* Advances Space in Research, 2008. 41(5): p. 1039-1045.
4. Dever, J.A., et al., *Mechnical properties degradation of TEFLON FEP returned from the hubble space telescope*, in *36th Aerospace Sciences Meeting&Exhibit*. 1998.
5. Sen, L., et al., *A model to describe the size distribution of satellite breakup debris*, in *63rd International Astronautical Congress*. 2012: Naples, Italy.
6. Murakami, J., et al., *Micro-satellite impact tests to investigate multi-layer insulation fragments*, in *Space Systems Dynamics Laboratory*. 2008, Kyushu University.
7. Liou, J.-C. and J.K. Weaver. *Orbital Dynamics of High Area-To Ratio Debris and Their Distribution in the Geosynchronous Region*. in *Proceedings of the 4th European Conference on Space Debris*. 2005. Darmstadt, Germany.
8. Valk, S., A. Lemaitre, and L. Anselmo, *Analytical and semi-analytical investigations of geosynchronous space debris with high area-to-mass ratio.* Advances in Space Research, 2008. 41.
9. Valk, S. and A. Lemaître, *Semi-analytical investigations of high area-to-mass ratio geosynchronous space debris including Earth's shadowing effects.* Advances in Space Research, 2008. 42.
10. Valk, S., A. Lemaître, and F. Deleflie, *Semi-analytical theory of mean orbital motion for geosynchronous space debris under gravitational influence.* Advances in Space Research, 2008. 43(7): p. 1070-1082.
11. Früh, C. and T. Schildknecht, *Attitude Motion of Space Debris Objects Under Influence of Solar Radiation Pressure And Gravitiy*, in *63rd international Astronautical congress*. 2012: Naples, Italy.
12. Früh, C., T.M. Kelecy, and M.K. Jah, *Coupled Orbit-Attitude Dynamics of High Area-to-Mass Ratio (HAMR) Objects: Influence of Solar Radiation Pressure, Shadow Paths and the Visibility in Light Curves.* Celestial Mechanics and Dynamical Astronomy (CELE), 2013.

13. Früh, C. and M. Jah, *Coupled orbit-attitude motion of high area-to-mass ratio (HAMR) objects including efficient self-shadowing*. Acta Astronautica, 2014. 95: p. 227-241.
14. Früh, C., et al. *Passive Electrostatic Charging of Near-Geosynchronous Space Debris HAMR Ojects and its Effects on the Coupled Object Dynamics*. in *Proc. AAS Space Flight Mechanics Meeting*. 2014. Santa Fe, NM.
15. McMahon, J.W. and D.J. Scheeres. *High-fidelity solar radiation pressure effects for high area-to-mass ratio debris with changing shapes*. in *Proceeding AAS/AIAA Astrodynamics Specialist Conference*. 2013. Hilton Head Island, South Carolina Paper AAS 13-763.
16. Channumsin, S., M. Ceriotti, and G. Radice, *A Deformation model of Flexible, high area-to-mass ratio debris for accurate propagation under perturbation*, in *65th International Astronautical Congress*. 2014: Toronto, Canada.
17. Sheldahl. *The red book*. 2012; Available from: http://www.sheldahl.com/documents/RedBook%20revised%2020-AUG%20%202012.pdf.
18. CAPLINQ, *Technical Data Sheet LINQSTAT PIT1N-ALUM SERIES*. 2012.
19. Batchelor, G.K., *An Introduction to Fluid Dynamics*. 1967: Cambridge University Press.
20. Holmes, J., *Wind Loading of Structures*. 2007, USA and Canada: Taylor & Francis.
21. Kalman, R.E., *A new approach to linear filtering and prediction problems.* Transaction of the ASME-Journal of Basic Engineering, 1960: p. 35-45.
22. Grewal, S. and P. Andrews, *Kalman Filtering Theory and Practice Using Matlab Grewal*, ed. n. Edition. 2001, New York: John Wiley & Sons Inc.
23. Suliman, C., C. Cruceru, and F. Moldoveanu, *Kalman Filter Based Tracking in an Video Surveillance System*, in *10th International Conference on Development and application systems*. 2010: Suceava, Romania.
24. Kalman, R.E., *A New Approach to Linear Filtering and Prediction Problems.* Journal of Basic Engineering, 1960. 82: p. 35-45.
25. Rafat, M.Z., M.S. Wheatland, and T.R. Bedding, *Dynamics of a double pendulum with distributed mass.* American Journal of Physics, 2009.
26. Eurolite, *Instruction Manual Theatre Spot 2000 Antihalo bk.* 2015.
27. MICRO-EPSILON, *Instruction Manual optoNCDT 1700*, http://www.micro-epsilon.com/download/manuals/man--optoNCDT-1700--en.pdf, Editor. 2014.
28. Vallado, D.A., *Fundamentals of Astrodynamics and Applications*. 2007, New York: Microcosm Press.